M. BAUER[1],✉
C. WIEMANN[2]
J. LANGE[3]
D. BAYER[3]
M. ROHMER[3]
M. AESCHLIMANN[3]

Phase propagation of localized surface plasmons probed by time-resolved photoemission electron microscopy

[1] IEAP, Christian-Albrechts Universität zu Kiel, Leibnizstr. 19, 24098 Kiel, Germany

[2] Forschungszentrum Jülich, Leo-Brandt-Str., 52425 Jülich, Germany

[3] Fachbereich Physik, University of Kaiserslautern, Erwin-Schrödinger Str. 46,
67663 Kaiserslautern, Germany

ABSTRACT In combining time-resolved two-photon photoemission (TR-2PPE) and photoemission electron microscopy (PEEM) the ultra-fast dynamics of collective electron excitations in silver nanoparticles (localized surface plasmons – LSPs) is probed at fs and nm resolution. Here we demonstrate that the sampling of the LSP dynamics by means of time-resolved PEEM enables detailed insight into the propagation processes associated with these excitations. In phase-integrated as well as phase-resolved measurements we observe spatio-temporal modulations in the photoemission yield from a single nanoparticle. These modulations are assigned to local variations in the electric near field as a result of the phase propagation of a plasmonic excitation through the particle. Furthermore, the control of the phase between the fs pump and probe laser pulses used for these experiments can be utilized for an external manipulation of the nanoscale electric near-field distribution at these particles.

PACS 78.47.+p; 78.67.Bf; 79.60.-i; 73.20.Mf

1 Introduction

The physics of localized collective electronic excitations in metallic nanostructures (often referred to as localized surface plasmons (LSPs) or Mie plasmons) has attracted considerable attention for decades. The complex electromagnetic fields induced at the surface, particularly at excitation in or close to the resonance of these LSPs, are thought to be responsible for the enhancement of nonlinear effects such as surface enhanced Raman scattering (SERS), surface second harmonic generation and multi-photon photoemission. Further interest in this field has been stimulated recently by the potential of surface plasmons to concentrate and channel light inside subwavelength structures to be used in nanoscopic photonic circuits [1, 2]. An unambiguous experimental access to the physics of LSP resonances, particularly with respect to nanoscale shape and size effects, typically requires well-defined and monodisperse nanostructured samples which are then addressed using lateral integrating techniques [3–7]. Alternatively, microscopy techniques directly or indirectly sensitive to LSPs may be applied to locally map the plasmon

✉ Fax: +49-431-880-1685, E-mail: bauer@physik.uni-kiel.de

properties with the advantage that heterogeneous particle distributions can be reasonably addressed [8, 9].
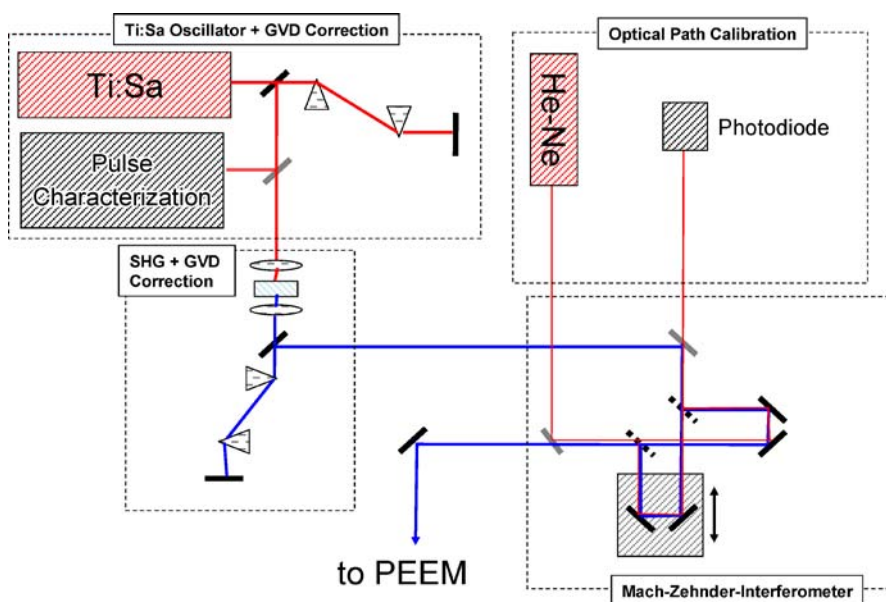
Photoemission electron microscopy (PEEM) in combination with nonlinear photoemission has just recently attracted considerable attention due to its high sensitivity to local LSP excitations combined with a lateral resolution in the sub-100-nm regime [10–14]. As the photoemission yield is governed by the local electric field distribution it can be used as a direct probe of the LSP-induced field enhancement. Another highly promising aspect is the potential of two-photon photoemission (2PPE) electron microscopy (2P-PEEM) to be performed in a time-resolved stroboscopic mode (TR-PEEM) enabling real-time experiments at a temporal resolution in the sub-100-fs regime [15]. This allows one to directly monitor the spatio-temporal dynamics of the local field distribution associated with the decay of the LSP mode. Even more, in a phase-resolved 2PPE mode (PR-PEEM) accurate information on the relative phase of the LSP mode to an oscillating reference field such as the driving external light field can be achieved [16]. This allows one to obtain a more complete picture of the near-field dynamics associated with plasmon excitations in low-dimensional nanostructures.

In this paper we exemplify the potential of TR-PEEM and PR-PEEM in probing the plasmon dynamics in nanostructured materials. By mapping the spatio-temporal evolution of the 2PPE yield within a single particle we are able to follow the phase propagation of a LSP through a particle on a sub-fs time scale. This example furthermore illustrates how the phase control of a laser field enables the manipulation of the local field distribution in nanoscopic systems.

2 Experimental

A schematic view of the experimental setup is shown in Fig. 1. The PEEM instrument used for our experiments (Focus IS-PEEM) is described in detail elsewhere [17]. The microscope is mounted in a ultrahigh vacuum (UHV) chamber which is constructed from μ-metal to shield external stray magnetic fields that would affect the imaging quality of the system with respect to the lateral resolution. The resolution that can be achieved with the microscope has been specified to be less than 40 nm. Two different light sources are available to record PEEM images: a conventional mercury vapor lamp UV source (high-energy cutoff at 4.9 eV)

and the frequency-doubled output of a fs Ti:sapphire laser system (800 nm, 80-MHz repetition rate, 30-fs pulse width (FWHM)). Using the mercury vapor lamp, the lateral distribution of the near-threshold photoemission is imaged by the PEEM. At a typical work function of the investigated silver nanostructures of about 4.5 eV the photon energy of the pulsed laser source ($h\nu = 3.1$ eV) is not sufficient for conventional photoemission. The high peak intensities of the fs pulses give rise, however, to high nonlinear 2PPE yields resulting in emission currents that are comparable to or even higher than those achieved in threshold photoemission with the mercury vapor lamp. The time-resolved and phase-resolved experiments are realized in a pump–probe configuration using a Mach–Zehnder type autocorrelator setup. Both pump and probe pulses are parallel linear polarized and have equal power at a photon energy of 3.1 eV. A complete measurement is performed by recording a series of images at varying temporal delays between the pump and the probe beams. For (phase-averaged) TR-PEEM measurements we use a mechanical delay stage with a positioning accuracy of 0.1 μm. The phase-resolved PEEM experiments were performed using a piezo-driven optical delay stage where the optical pathway is calibrated by monitoring the interference pattern of a counter-propagating He–Ne laser beam. The beam of a frequency-stabilized He–Ne oscillator is coupled into and out of the interferometer through dielectrically coated mirrors, which are highly reflective at the pump/probe wavelength of 400 nm, but yield good transparency at the He–Ne laser wavelength of 632 nm. The monitoring beam travels through the interferometer on the same optical pathway as the pump/probe beam and is likewise split and recombined. The intensity of the interference between the two pathways of the monitoring beam is recorded by a photodiode and used to calculate the actual difference in optical path length between the two interferometer arms at each measurement position. The latter setup guarantees maximum accuracy in the relative positioning of both interferometer arms of 20 nm, corresponding to a temporal delay between the respective laser pulses traveling through the different arms of 67 as. This allows for high-resolution sam-

pling of the local field interferences at the surface, induced by the 400-nm light (oscillation period: 1.3 fs). The performance of the interferometer has been checked by lateral integrating phase- and time-resolved 2PPE measurements from a poly-crystalline tantalum sheet (see Fig. 2). The displayed data were recorded using an electron energy analyzer (Focus CSA) mounted in a different UHV chamber at an electron kinetic energy of 6 eV (sample bias: -4 V with respect to analyzer entrance) close to the high-energy cutoff of the 2PPE spectrum. The oscillation fringes due to the interference between pump and probe pulses are clearly resolved and the accurate
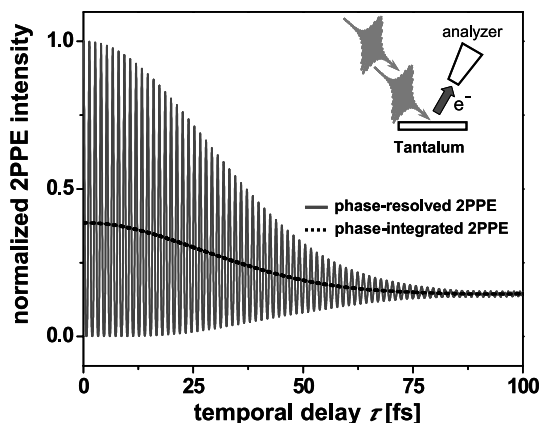
FIGURE 2 Time- and phase-resolved 2PPE from a polycrystalline tantalum sheet measured at an electron kinetic energy of 6.0 eV. The *gray line* is the measured 2PPE interferogram; the *black dashed line* shows for comparison data as achieved in a conventional (phase-integrated) 2PPE measurement
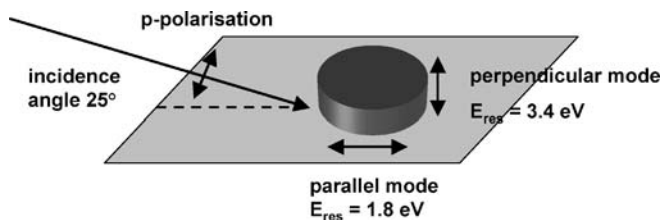
FIGURE 3 Excitation geometry and LSP modes in a cylindrical nanoparticle
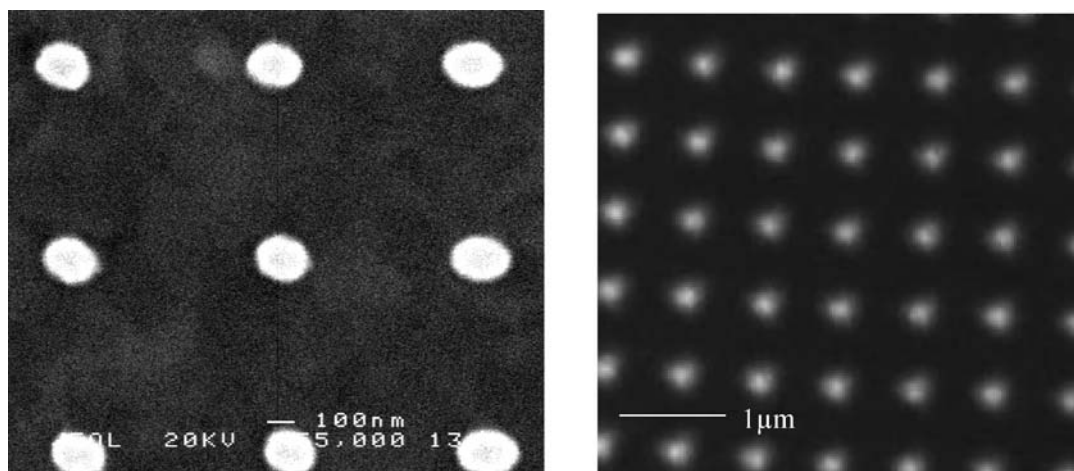
FIGURE 4   *Left*: SEM image of the nanodot sample; *right*: PEEM image (field of view: 4.5 μm) of the silver sample recorded in threshold photoemission ($h\nu = 4.9$ eV); the periodicity of the nanodot array is 750 nm, the height of a single particle is 50 nm, the diameter is 200 nm

periodicity reproduced for these measurements over the entire temporal delay proves the position stability of the setup used.

Small silver particles deposited on a 30-nm-thick ITO substrate on top of a 1-mm-thick glass disk were prepared using electron-beam lithography as described in [18]. This procedure allows for controlled design of periodic arrays of nanoparticles at varying shapes and distances down to the sub-50-nm regime. For the present study a periodic array (size: $150\,\mu\text{m} \times 150\,\mu\text{m}$, periodicity: 750 nm) consisting of silver nanoparticles (height: 50 nm, diameter: 200 nm) has been prepared. A scanning electron microscope (SEM) image and a PEEM image recorded in threshold photoemission of the sample ($h\nu = 4.9$ eV) are shown in Fig. 4. The SEM image shows that particle to particle variations in size and form are negligible, demonstrating the homogeneity of the lithography process. Past studies concerning the optical properties of such structures and performed at similar wavelength have also shown a very homogeneous response of such particle ensembles [19]. In the PEEM, the periodicity of the particle array is well imaged, as is the size of the particles, if the finite resolution of the microscope is taken into account. The instrument is specified to reach a spatial resolution below 40 nm. However, owing to the peculiarities of the image formation in an emission microscope, the resolution is influenced heavily by sample topography. Since the sample surface is conducting, the equipotential surfaces of the objective lens's acceleration field follow the surface topography in the vicinity of the sample, causing inhomogeneities in the electric field. These field inhomogeneities deflect photoelectrons near the surface, thereby generating the well-known topography contrast in PEEM. On the downside, they decrease the instrumental resolution. For a more detailed analysis of surface field effects in PEEM, see for example [20].

The LSP resonances of silver nanoparticles are generally located in the optical regime and depend on the size and shape of the particle, and the dielectric response of the environment surrounding the particle [21]. Since the particles are circular cylinders, they exhibit two plasmon resonances (one of which is twofold degenerate), see Fig. 3. The perpendicular mode is due to the movement of charges in the direction perpendicular to the substrate, along the cylinder axis. Model calculations based on the work of Kuwata et al. [22] predict the resonance energy of this mode to be 3.4 eV. The two modes parallel to the substrate surface are energetically degenerate due to the circular symmetry of the particles. Their resonance energy can be found by extinction spectroscopy at normal incidence to be 1.8 eV, in agreement with the model calculations. Our calculations are therefore also a reliable estimate of the resonance energy of the perpendicular plasmon mode. We conclude that for p-polarized excitation[1] with the 400-nm laser light ($h\nu = 3.1$ eV) a resonant or near-resonant excitation of the perpendicular mode is accomplished.

3   Results and discussion

3.1   *Phase-integrated time-resolved PEEM results*

Figure 5a shows a two-photon photoemission map of the sample recorded at $h\nu = 3.1$ eV with p-polarized laser light. The periodic nanodot array is clearly resolved. The silver particles are the dominating photoemitters, whereas the photoemission yield from the ITO interstitial areas is of the order of the background signal (microchannel plate (MCP) and charge-coupled device (CCD) detector noise) or below. The inhomogeneity in the local 2PPE yield from different dots is related to statistical variations in the density of structural imperfections (lattice defects) of the nanoparticles. Such imperfections act as momentum sources for Landau damping processes (decay of plasmons due to the creation of electron–hole pairs) and support intraband excitations required for the 2PPE emission from noble-metal particles [23]. As the decay of the LSP mode for particle dimensions as studied in this work is dominated by radiation damping [24], this variable contribution to the Landau damping efficiency barely affects the total fs dynamics related to the plasmon excitations and the consequent field enhancement in the nanoparticles. This insensitivity is, for instance, evidenced by the homogeneous line width of the plasmon resonance deduced from lateral integrating extinction spectra at equivalent samples [25].

---

[1] For p-polarized light the electric field vector of the incident laser pulse is oriented parallel to the plane defined by the normal of the substrate surface and the *k*-vector of the laser pulse.
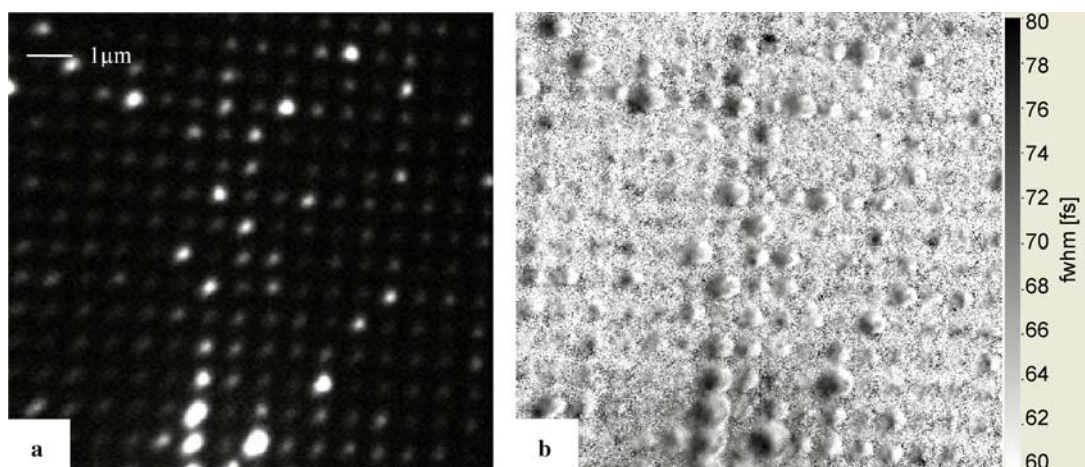
FIGURE 5 (**a**) The two-photon photoemission yield ($h\nu = 3.1$ eV) from the nanodot array mapped with 2P-PEEM; (**b**) corresponding FWHM map deduced from a local analysis of the autocorrelation traces recorded in a time-resolved PEEM scan. Field of view: 11 μm. For details see text

The first experiments to map the local fs dynamics related to the perpendicular plasmon mode of the particles have been performed within time-resolved PEEM experiments in the phase-integrated mode. These experiments already show residuals of the complexity of the collective electron dynamics, which will be analyzed later in this paper in more detail based on phase-resolved PEEM results. To visualize the lateral variations in the electron dynamics probed in this experiment, we performed a point-to-point analysis of the images recorded in the time-resolved PEEM scans. A measure for the dynamics involved in the collective excitation of electrons by the fs laser pulse is the FWHM of the 2PPE autocorrelation trace (AC trace). Note that the FWHM of the AC trace is not simply the lifetime of the collective excitation, but contains a convolution of the laser pulse autocorrelation and the dynamics of electron–hole excitations as well as the dynamics of the plasmon excitation. We extract this quantity from a sech^2 fit to the AC trace of each image pixel as recorded in the pump–probe scan. The display of these FWHMs in a gray-scale map (FWHM map, see Fig. 5b) gives an intuitive view of the systematic variations in the fs dynamics related to local electron excitations in the nanoparticle array. The dynamics involves the decay of plasmon modes and single-electron excitations as well as the propagation of plasmons, as will be discussed later. In Fig. 5b, the periodic structure of the sample is also clearly reproduced. The apparent enlargement of the nanodots in the FWHM map in comparison to the 2PPE image arises from a lateral constant FWHM signal which is independent of the 2PPE-intensity profile of a single nanodot as long as the count statistics allows for a reasonable sech^2 fit (see for instance Fig. 8b). At lower count rates on the order of the signal-background level, the sech^2 fits are no longer reliable so that for dim nanodots as well as the interstitial ITO areas the actual AC-FWHM related to the fs dynamics becomes significantly blurred.

To obtain information on systematic effects related to the probed particle plasmon dynamics a statistical analysis of the FWHM map has been performed. Figure 6a shows the number of particles as a function of the measured FWHM. For this diagram only particles that can be clearly separated from the background in the 2PPE image (Fig. 5a) have been considered. The FWHM has been obtained from the center area of the nanoparticle. A Gaussian fit to this distribution (dashed line) gives a mean value of the FWHM of the AC trace of 67 fs with a spread of 7 fs. This scatter is consistent with an error of ± 2 fs for the accuracy in the analysis of the local AC traces
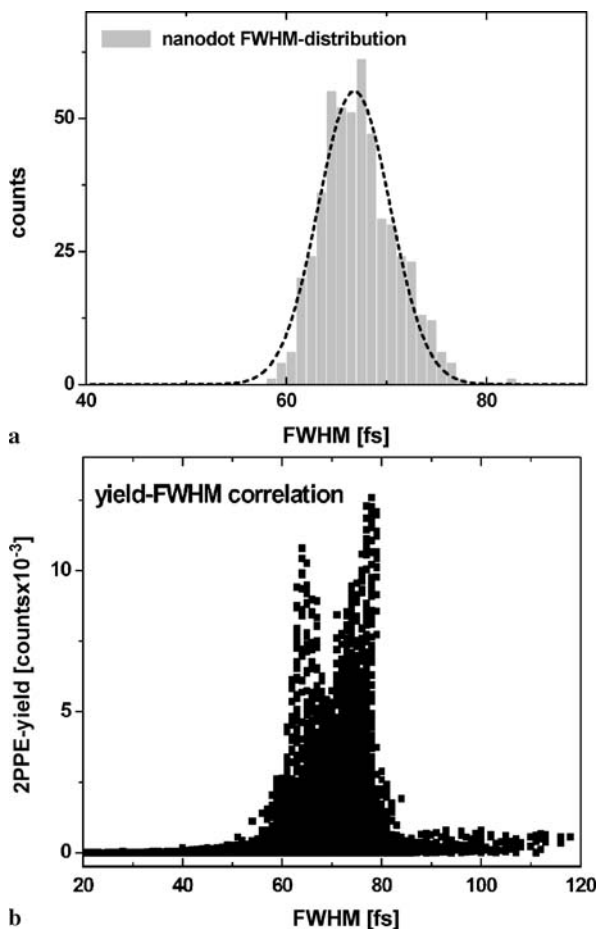
FIGURE 6 Correlation diagrams extracted from Fig. 5b: (**a**) number of particles as a function of the FWHM of the autocorrelation trace at the center of the particle; (**b**) correlation between 2PPE yield and measured FWHM of the autocorrelation trace (all points in Fig. 5b have been considered)
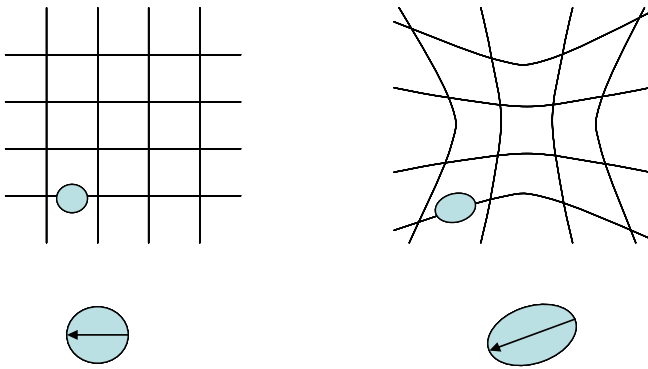
FIGURE 7   Effect of image distortion on the observed direction of propagation

and indicates a rather homogeneous (particle-independent) dynamical response of the nanoparticle array. The general picture becomes more complex if we examine the correlation between the 2PPE intensity and the AC-FWHM as displayed in Fig. 6b. For this analysis all data points of the PEEM image have been considered. We observe a structured correlation diagram exhibiting two distinct maxima at FWHM values of 63 fs and 74 fs. At first glance it is tempting to interpret such a bifurcation in terms of two different particle species at the sample exhibiting a different dynamical response to the exciting laser field. A comparison between the 2PPE-intensity map (Fig. 5a) and the FWHM map (Fig. 5b) excludes this explanation. The splitting in the FWHM distribution in Fig. 6b is obviously governed by the most intense particles. The dynamical response of these particles as represented in the FWHM map is, however, rather similar. Furthermore, the existence of such a distinction between particles should also appear in the frequency distribution of FWHM values displayed in Fig. 6a. We find instead that the observable splitting is intrinsic to the particle property and arises from a left–right asymmetry in the FWHM response of the individual particles. We can assign these two peaks to the systematic dark–bright modulation of the individual particles, which is clearly visible in the FWHM map (Fig. 5b). The left-hand area of a particle typically exhibits a larger FWHM than the right-hand area. The

deviation from this left–right asymmetry to a bottom-left to top-right asymmetry for particles located at the image bottom arises from image distortion, see the illustration in Fig. 7. The relevant image defect in this case is known as pincushion distortion and is described in [26] as the dominant geometric defect of projectors. It is possible to find voltage settings that minimize image distortion at a given magnification, but a residue will always be present in the image, especially at the edges, because the effect increases radially proportional to r^3 (distance from the optical axis to the third power).

In Fig. 8a, AC traces from three different locations within a single nanoparticle are directly compared. The difference in the dynamical response is evident. Figure 8b compares the measured FWHM along the center axis of a particle with the corresponding 2PPE-intensity profile of the nanoparticle. The response of a single particle to the fs laser pulse is obviously not characterized by a single 2PPE autocorrelation but by a dynamical response which varies locally across the nanoparticle. The actual origin of this asymmetry is not directly evident from the phase-integrated measurements but requires more detailed phase-resolved 2P-PEEM investigations as presented in Sect. 3.2. However, we note at this point that for the presented data the laser field impinges onto the nanoparticle field from the right-hand side at an angle of 25° with respect to the surface. This grazing incidence of the excitation light may give rise to the broken symmetry required for the observation of such a directional and systematic variation in the measured FWHM value effect.
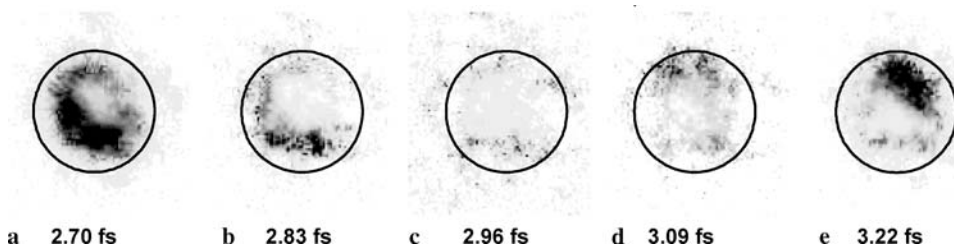
3.2   *Phase-resolved PEEM results*

The origin of the systematic particle asymmetry in the excitation dynamics as identified in the time-resolved PEEM experiments becomes more evident in phase-resolved PEEM measurements. Figure 9 shows a section of a PR-PEEM scan (interferogram) of a selected particle (image size: 420 nm × 420 nm), which covers a time regime corresponding to two oscillation periods of the exciting 400-nm laser light. The temporal delay between two consecutive images is 130 as. The visible (periodic) intensity oscillations result from
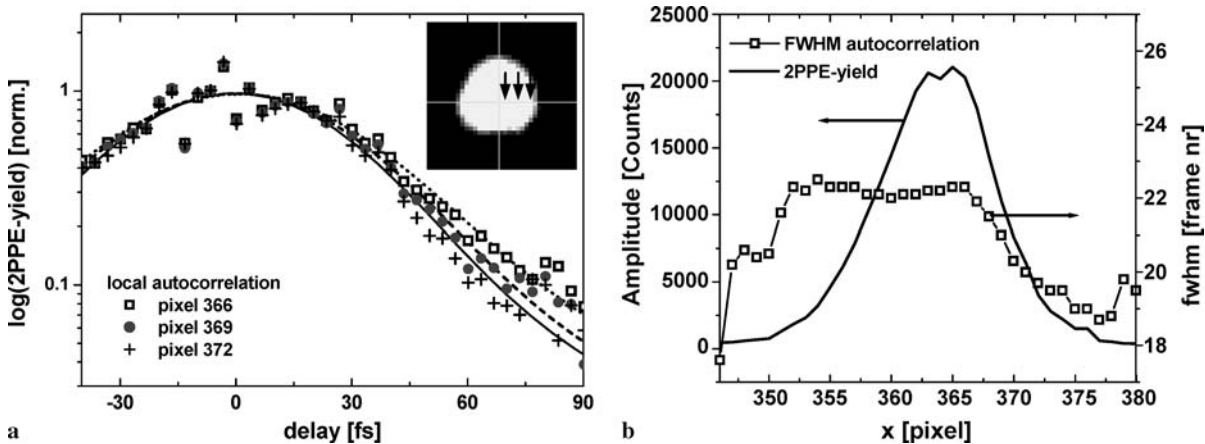
FIGURE 8   (**a**) Comparison of local 2PPE autocorrelations of a single nanodot; the corresponding positions are indicated in the *inset* by the *arrows*; (**b**) autocorrelation FWHM distribution of a nanodot (in units of the image number of the pump-probe scan) in comparison to the intensity profile in the center of the particle (the position is given by the pixel number of the CCD detector); note the pronounced asymmetry of the FWHM trace with respect to the 2PPE-intensity profile
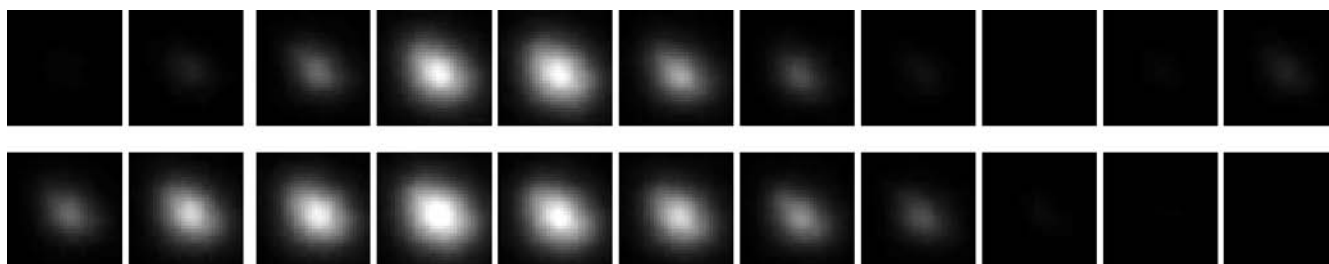
FIGURE 9   Section of a single-particle phase-resolved PEEM scan at an excitation energy of 3.1 eV. The images are displayed at a temporal delay rate of 0.14 fs/frame, the image size is 420 nm × 420 nm

a   2.70 fs   b   2.83 fs   c   2.96 fs   d   3.09 fs   e   3.22 fs

FIGURE 10   Phase-resolved PEEM scan of a single particle of the sample (particle diameter: 200 nm) highlighting particle internal 2PPE-yield variations as a function of the temporal delay between pump and probe laser pulses

alternating constructive and destructive interference between pump and probe laser pulses when the temporal delay (or, alternatively speaking, the phase delay) between both pulses is scanned. In this context it is important to note once again that the actual electron emission from the particle is not governed by the external laser field but rather by the internal particle near field related to the excitation of the LSP resonance by the laser field [27]. Therefore, next to the pump–probe interference, the variation in the electron emission yield also contains the information on the response of the LSP-induced near field to the driving external laser field.

To highlight the internal asymmetry of particles as observed in the phase-integrated measurements (and their modification as a function of phase delay), Fig. 10 shows a 2PPE-yield map from a selected particle at varying delays (0.13-fs time steps per image frame). To enhance the small but significant variations in the delay-dependent 2PPE-intensity distribution the image displays the 2PPE signal normalized by the corresponding local 2PPE yield recorded at time zero. Thus, any contributions to 2PPE-intensity variations due to static (non-delay-dependent) particle inhomogeneities related to known contrast mechanisms (such as topography, defects or work-function variations) are canceled. The residual signal is directly related to the local near field associated with the LSP and governing the 2PPE emission. Clearly visible is a modification of the local intensity distribution as a function of the temporal delay between pump and probe pulses. The image series implies that the intensity maximum of the 2PPE yield propagates from the top-right to the bottom-left area of the particle within a third of the oscillation period of the driving external electromagnetic field. Note that the lateral response of the particle is again slightly distorted by the image defects of the projectors (see bottom particles in Fig. 5b). We conclude that the propagation direction of the local field distribution as probed in the phase-resolved measurement agrees with the particle asymmetry already identified in the conventional TR-PEEM scans.

A quantitative analysis of these PR-PEEM results is displayed in Fig. 11. The graph compares laterally integrated 2PPE intensities from the top-right area (area B) and the bottom-left area (area A) of the particle as a function of temporal delay over two oscillation periods of the laser field (see inset in Fig. 11). The phase shift in the response of area B in comparison to area A is clearly visible. The phase slip across the particle is about $\pi/15$. It is not restricted to the oscillations close to time zero, as shown in Fig. 11, but stays constant over the entire delay range probed in the experiment.

The origin of the nanoparticle internal phase dynamics becomes obvious if the off-normal (grazing incidence) laser illumination of the particles is considered, which is typically used in a PEEM experiment. This symmetry break in the light–particle interaction is a prerequisite for the observation of a modulation in the lateral single-particle 2PPE-yield distribution. Consider the laser light as a plane wave incident from the right onto a particle where the electric field amplitude is determined by the phase delay $\Delta\varphi(\tau)$ between pump and
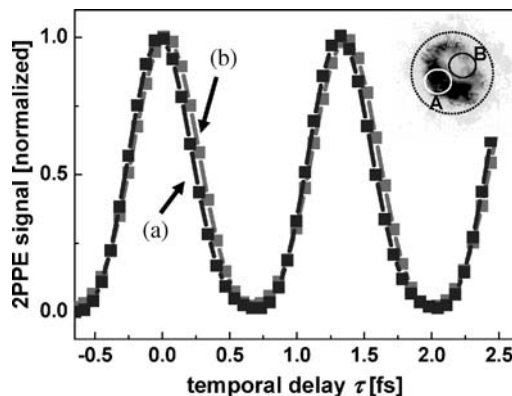
FIGURE 11   Comparison of interferograms taken from different areas (A and B, see *inset*) of the particle shown in Fig. 9

probe pulses as adjusted by the Mach–Zehnder interferometer. For the following it is unnecessary to consider the pulsed structure of the laser light, so that the relevant temporal dependence of the total incident oscillating electric field $E_{\text{tot}}(t)$ can be written as

$$E_{\text{tot}}(t) = E_1 e^{i\omega t} + E_2 e^{i\omega t + \Delta\varphi(\tau)} . \tag{1}$$

Here, E_1 and E_2 are the amplitudes of the pump and probe laser fields and ω is the oscillation frequency corresponding to the photon energy used of $h\nu = 3.1$ eV. Incident from the right, we expect the laser light to couple at first to the LSP mode at the right-hand edge ($r = 0$) of the particle. In a one-dimensional view this will induce a locally oscillating field $E_{\text{LSP}}(t, r = 0)$ of the form

$$\begin{aligned} E_{\text{LSP}}(t, r = 0) &= A(\omega) e^{i\delta(\omega)} E_{\text{tot}}(t) \\ &= A e^{i\delta(\omega)} \left(E_1 e^{i\omega t} + E_2 e^{i\omega t + \Delta\varphi(\tau)} \right) . \end{aligned} \tag{2}$$

Here, $A(\omega)$ can be considered as the field enhancement factor of the external field due to the coupling to the LSP mode. The phase $\delta(\omega)$ is the (frequency-dependent) phase shift of the LSP response to the external field. $E_{\text{LSP}}(t, r = 0)$ is the field that governs the measured 2PPE yield from the right-hand part of the particle mapped by the PEEM. The periodic variation in the local 2PPE intensity as a function of time directly reflects the change between constructive and destructive interference of the pump and probe laser beams as the phase delay $\Delta\varphi$ (the Mach–Zehnder interferometer, respectively) is scanned. The phase of both fields, $E_{\text{tot}}(t)$ and $E_{\text{LSP}}(t, r = 0)$, will propagate along the particle, however, at different phase velocities. The external light field $E_{\text{tot}}(t)$ will give rise to a locally varying particle field $E'_{\text{LSP}}(t, r)$ of the form

$$E'_{\text{LSP}}(t, r) = A'(\omega, r) e^{i(\delta(\omega) + \varrho(r))} E_{\text{tot}}(t) . \tag{3}$$

Here, r denotes the location at the particle and $\varrho(r) = \omega/cr$ is the phase difference with respect to the 'right-hand edge' LSP field $E_{\text{LSP}}(t, r = 0)$ governed by the phase velocity c of the vacuum plane wave. In a similar manner, the field induced at the particle position r by the propagating LSP mode can be written as

$$E_{\text{LSP}}(t, r) = A(\omega, r) e^{i(\delta(\omega) + \varrho_{\text{LSP}}(r))} E_{\text{tot}}(t) , \tag{4}$$

where $\varrho_{\text{LSP}}(r) = \omega/v_{\text{LSP}}r$ is the propagation-induced phase delay of $E_{\text{LSP}}(t, r)$ with respect to $E_{\text{LSP}}(t, r = 0)$, this time governed by the phase velocity v_{LSP} of the plasmon mode in the particle. The total 2PPE yield at a given position r is determined by the interference between the fields $E'_{\text{LSP}}(t, r)$ and $E_{\text{LSP}}(t, r)$. For a given pump–probe delay τ the detailed interference depends on the local phase difference $\varrho(r) - \varrho_{\text{LSP}}(r)$, so that we generally expect the overall local field amplitude $E'_{\text{LSP}}(t, r) + E_{\text{LSP}}(t, r)$ to vary with position r. Only for $\varrho(r) = \varrho_{\text{LSP}}(r)$ would the phase difference between $E'_{\text{LSP}}(t, r)$ and $E_{\text{LSP}}(t, r)$ and consequently the total local field stay constant over the entire particle. In general, we expect the phase velocity v_{LSP} of the collective excitation to be smaller than the vacuum phase velocity c of light, giving rise to a phase loss between the two fields and resulting in the local 2PPE-intensity modulations as observed in the experiment (Fig. 10). By this means, the particle internal structure visible in a single PEEM image of Fig. 10 is a residual of the interference between the external light field and the particle characteristic LSP field. As $\varrho(r)$ is exclusively governed by the well-known vacuum properties of the incident laser light we can, in principle, deduce the magnitude of the LSP phase velocity v_{LSP} from these intensity modulations. For an accurate estimate, however, a phase shift between the external light wave and the LSP mode of at least π along the particle extension is required. This is not the case for the short (200-nm) particles in this study, but requires larger (preferably elongated) particles.

So far, we have considered the case of a fixed phase delay $\Delta\varphi$ (fixed temporal delay τ) between pump and probe pulses. The variation of the temporal delay τ between the two light pulses in our phase-resolved 2PPE experiments offers a further (external) degree of freedom with respect to the phase properties and therefore the local interference conditions of the entire electric field at the nanoparticle. As we can see from a comparison of different images recorded at varying τ, this additional phase contribution enables an efficient manipulation of the particle internal local electric field distribution. Comparison of Fig. 10a and e shows, for example, that the maximum field amplitude can be shifted from one side of the particle to the other. We therefore consider the adjustment of the relative phase between pump and probe pulses by the Mach–Zehnder interferometer as an efficient means of a coherent manipulation of the local electric field distribution in nanoscale structures. In another PEEM experiment an efficient approach for a controlled manipulation of the local field distribution (field enhancement) has just recently been demonstrated by means of a defined structuring of nanoscale particles [11]. The use of coherent light pulses for a nanoscale control of local fields has been predicted theoretically in several publications [28, 29]. The results presented here are an experimental example for such a control scenario. We propose that the combination of structuring and coherent control of the exciting light may lead to high flexibility in the nanoscale manipulation of local electric fields. The photoemission electron microscopy can play a key role in identifying these effects.

4   Conclusions

Femtosecond time-resolved photoemission electron microscopy has the potential to become one of the leading techniques in the real-time imaging of ultra-fast processes at nanostructured surfaces. The two experimental examples presented in this paper highlight the capability of time-resolved and phase-resolved PEEM to map fs dynamics associated with plasmon excitations at sub-wavelength resolution. The parallel image acquisition of PEEM guarantees the resolution of small lateral variations in the local dynamical behavior. The obtained evidence of a phase propagation of a plasmon mode through an extended nanoparticle is a first step towards a direct imaging of the ultra-fast dynamics of energy flow through nanoscopic devices. This is an important step towards the understanding and the optimization of nanoscopic photonic circuits. Another aspect addressed in this paper is the external manipulation of the lateral near-field distribution in nanoscale structures by the phase control of the ex-

citing fs laser field. We have demonstrated that PEEM is the technique of choice to visualize and prove such a control scenario.

REFERENCES

1 A.V. Zayats, I.I. Smolyaninov, J. Opt. A Pure Appl. Opt. **5**, 16 (2003)
2 W.L. Barnes, A. Dereux, T.W. Ebbesen, Nature **424**, 824 (2003)
3 B. Lamprecht, G. Schider, R.T. Lechner, H. Ditlbacher, J.R. Krenn, A. Leitner, F.R. Aussenegg, Phys. Rev. Lett. **84**, 4721 (2000)
4 S. Linden, J. Kuhl, K. Giessen, Phys. Rev. Lett. **86**, 4688 (2001)
5 J. Lehmann, M. Merschdorf, W. Pfeiffer, A. Thon, S. Voll, G. Gerber, Phys. Rev. Lett. **85**, 2921 (2000)
6 H. Hövel, S. Fritz, A. Hilger, U. Kreibig, M. Vollmer, Phys. Rev. B **48**, 18 178 (1993)
7 F. Stietz, J. Bosbach, T. Wenzel, T. Vartanyan, A. Goldmann, F. Träger, Phys. Rev. Lett. **84**, 5644 (2000)
8 J.-C. Weeber, J.R. Krenn, A. Dereux, B. Lamprecht, Y. Lacroute, J.P. Goudonnet, Phys. Rev. B **64**, 045 411 (2001)
9 C. Sönnichsen, T. Franzl, T. Wilk, G. von Plessen, J. Feldmann, O. Wilson, P. Mulvaney, Phys. Rev. Lett. **88**, 077 402 (2002)
10 M. Cinchetti, D.A. Valdaitsev, A. Gloskovskii, A. Oelsner, S.A. Nepijko, G. Schönhense, J. Electron Spectrosc. Relat. Phenom. **137–140**, 249 (2004)
11 M. Cinchetti, A. Gloskovskii, S.A. Nepjiko, G. Schönhense, H. Rochholz, M. Kreiter, Phys. Rev. Lett. **95**, 047 601 (2005)
12 G.H. Fecher, O. Schmidt, Y. Hwu, G. Schönhense, J. Electron Spectrosc. Relat. Phenom. **126**, 77 (2002)
13 M. Munzinger, C. Wiemann, M. Rohmer, L. Guo, M. Aeschlimann, M. Bauer, New J. Phys. **7**, 68 (2005)
14 L.I. Chelaru, M. Horn-von Hoegen, D. Thien, F.-J. Meyer zu Heringdorf, Phys. Rev. B **73**, 115 416 (2006)
15 O. Schmidt, M. Bauer, C. Wiemann, R. Porath, M. Scharte, O. Andreyev, G. Schönhense, M. Aeschlimann, Appl. Phys. B **74**, 323 (2002)
16 A. Kubo, K. Ondo, H. Petek, Z. Sun, Y.S. Jung, H.K. Kim, Nano Lett. **5**, 1123 (2005)
17 W. Swiech, G.H. Fecher, C. Ziethen, O. Schmidt, G. Schönhense, K. Grzelakowski, C.M. Schneider, R. Frömter, H.P. Oepen, J. Kirschner, J. Electron Spectrosc. Relat. Phenom. **84**, 171 (1997)
18 W. Gotschy, K. Vonmetz, A. Leitner, F.R. Aussenegg, Appl. Phys. B **63**, 381 (1996)
19 B. Lambrecht, J.R. Krenn, A. Leitner, F.R. Aussenegg, Appl. Phys. B **69**, 223 (1999)
20 S.A. Nepijko, N.N. Sedov, G. Schönhense, M. Escher, X. Bao, W. Huang, Ann. Phys. **9**, 441 (2000)
21 U. Kreibig, M. Vollmer, *Optical Properties of Metal Clusters* (Springer Ser. Mater. Sci. **25**) (Springer, Heidelberg, 1995)
22 H. Kuwata, H. Tamaru, K. Esumi, K. Miyano, Appl. Phys. Lett. **83**, 4625 (2003)
23 C. Wiemann, D. Bayer, M. Rohmer, M. Aeschlimann, M. Bauer, Surf. Sci., in print, DOI 10.1016/j.susc.2007.05.040
24 M. Scharte, R. Porath, T. Ohms, M. Aeschlimann, J.R. Krenn, H. Ditlbacher, F.R. Aussenegg, A. Liebsch, Appl. Phys. B **73**, 305 (2001)
25 B. Lamprecht, J.R. Krenn, A. Leitner, F.R. Aussenegg, Appl. Phys. B **69**, 223 (1999)
26 P.W. Hawkes, E. Kasper, *Principles of Electron Optics*, vol. 1: *Basic Geometrical Optics* (Academic, London, 1989)
27 M. Merschdorf, C. Kennerknecht, W. Pfeiffer, Phys. Rev. B **70**, 193 401 (2004)
28 M.I. Stockman, S.V. Faleev, D.J. Bergman, Phys. Rev. Lett. **88**, 067 402 (2002)
29 T. Brixner, F.J. García de Abajo, J. Schneider, W. Pfeiffer, Phys. Rev. Lett. **95**, 093 901 (2005)